Detailed seismic velocity of the incoming subducting sediments in the 2004 great Sumatra earthquake rupture zone from full waveform inversion of long offset seismic data

Yanfang Qin, Satish C. Singh

AGU PUBLICATIONS

Geophysical Research Letters

RESEARCH LETTER
10.1002/2016GL072175

Key Points:
- Elastic full waveform inversion is applied to long offset streamer seismic data that were acquired at North Sumatra subduction trench
- The inversion provides detailed *P* wave velocity information on the incoming oceanic sediments and the trench-fill sediments
- There is a low-velocity protodécollement layer above the highly compacted pelagic sediments, which could contribute to the 2004 tsunami

Supporting Information:
- Supporting Information S1

Correspondence to:
Y. Qin,
qin@ipgp.fr

Citation:
Qin, Y., and S. C. Singh (2017), Detailed seismic velocity of the incoming subducting sediments in the 2004 great Sumatra earthquake rupture zone from full waveform inversion of long offset seismic data, *Geophys. Res. Lett.*, *44*, 3090–3099, doi:10.1002/2016GL072175.

Received 27 JUN 2016
Accepted 16 MAR 2017
Accepted article online 20 MAR 2017
Published online 1 APR 2017

Detailed seismic velocity of the incoming subducting sediments in the 2004 great Sumatra earthquake rupture zone from full waveform inversion of long offset seismic data

Yanfang Qin[1] and Satish C. Singh[1]

[1]Equipe de Géosciences Marines, Institut de Physique du Globe de Paris (CNRS, Paris Diderot, Sorbonne Paris Cité), Paris, France

Abstract The nature of incoming sediments defines the locking mechanism on the megathrust, and the development and evolution of the accretionary wedge. Here we present results from seismic full waveform inversion of 12 km long offset seismic reflection data within the trench in the 2004 Sumatra earthquake rupture zone area that provide detailed quantitative information on the incoming oceanic sediments and the trench-fill sediments. The thickness of sediments in this area is 3–4 km, and *P* wave velocity is as much as ~4.5 km/s just above the oceanic crust, suggesting the presence of silica-rich highly compacted and lithified sediments leading to a strong coupling up to the subduction front. We also find an ~70–80 m thick low-velocity layer, capped by a high-velocity layer, at 0.8 km above the subducting plate. This low-velocity layer, previously identified as high-amplitude negative polarity reflection, could have porosity of up to 30% containing overpressured fluids, which could act as a protodécollement seaward from the accretionary prism and décollement beneath the forearc. This weak protodécollement combined with the high-velocity indurated sediments above the basement possibly facilitated the rupture propagating up to the front during the 2004 earthquake and enhancing the tsunami. We also find another low-velocity layer within the sediments that may act as a secondary décollement observed offshore central Sumatra, forming bivergent pop-up structures and acting as a conveyer belt in preserving these pop-up structures in the forearc region.

1. Introduction

Prior to the 2011 Tohoku earthquake, it was accepted that the frontal section of a subduction system behaves aseismically, incapable of storing seismic energy and producing a large slip [*Moore and Saffer*, 2001], even though there were suggestions for the rupture propagation to the front during the 2004 great Sumatra earthquake [*Henstock et al.*, 2006; *Singh et al.*, 2008; *Dean et al.*, 2010; *Gulick et al.*, 2011]. The nature of the incoming sediments along with the structural, rheological, or thermal conditions within plates control coupling along a megathrust. The coupling is defined as the ratio of slip rate over convergence rate during the interseismic period and is a measure of the degree of locking [e.g., *Konca et al.*, 2008]. For example, strong materials in the trench would lead to a strong coupling between the two plates, producing large slips during megathrust earthquakes [*Chester et al.*, 2012]. Furthermore, the properties and evolution of these input materials are directly linked to forearc structures that relate to the dynamic earthquake process [*Wang and Hu*, 2006]. Therefore, it is important to characterize the properties of these incoming sediments.

The most direct method to characterize these sediments is drilling, which is very expensive and can only be carried out on a few locations. An International Ocean Discovery Program drilling took place in August–October 2016 offshore Sumatra in the west Wharton Basin, near the Ninety East Ridge, about 200 km from the trench (Figure 1). Although these results would be extremely important, what happens to these sediments as they get buried beneath thick trench sediments and strongly affected by the subduction process would require drilling within the trench, which has not been done yet.

Seismic full waveform inversion [*Lailly*, 1983; *Tarantola*, 1984, 1986] could be used to determine the elastic properties of the subsurface. Here we apply full waveform inversion accompanied by some advanced analysis techniques to a 33 km long portion of a seismic profile near the trench to characterize the nature of these trench sediments (Figures 1 and S1 in the supporting information). The study area lies seaward of the Sumatra subduction zone where the maximum slip occurred during the 2004 great Sumatra earthquake

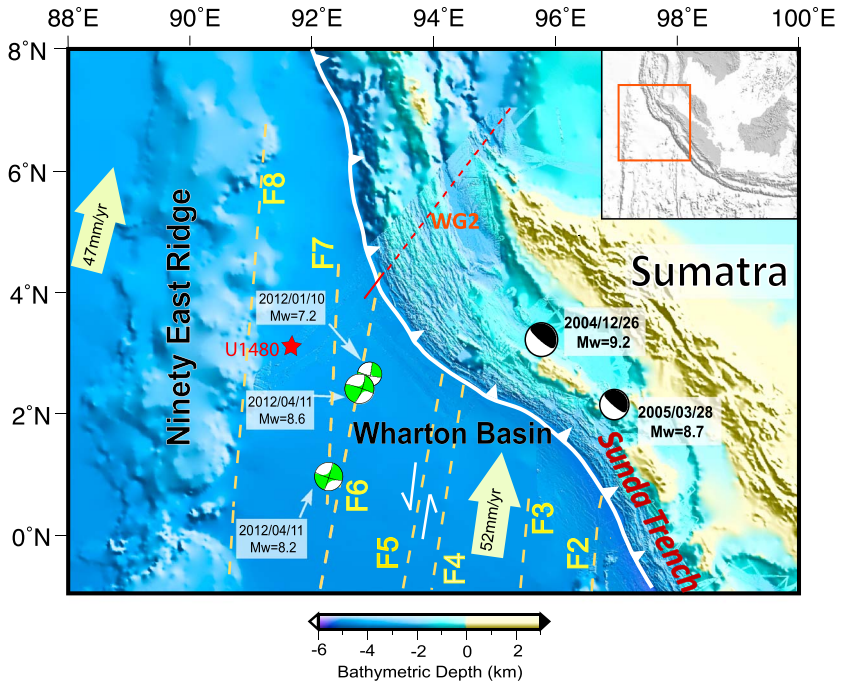

Figure 1. Seafloor bathymetry and island topography in the eastern Indian Ocean. The Sunda Trench is marked by a white line. The yellow dashed lines mark the fracture zones, which have a N9°E azimuth (F2–F8) and have been reactivated as left-lateral strike-slip faults [*Deplus et al.*, 1998; *Carton et al.*, 2014]. The earthquake sequence in 2012 is marked by the green beach balls, while the 2004 great Sumatra-Andaman megathrust $M_w = 9.2$ earthquake and 2005 Nias $M_w = 8.7$ earthquake off Sumatra are represented by black beach balls. The seismic line WG2 is marked by a red line; the solid part is our study region. The directions of the subducting plate are shown by yellow arrows. The red star represents the International Ocean Discovery Program drill site U1480 in August–October 2016.

[*Ammon et al.*, 2005]. The trench in this area consists of ~4 km thick sediments deposited over a 58 to 60 Ma old oceanic crust [*Moeremans et al.*, 2014; *Liu et al.*, 1983]. The sediments originated either by the denudation of the Himalaya mountain belt or by the erosion of the forearc high structures.

2. Prior Seismic Results

The existing seismic reflection data indicate that the trench off north Sumatra is filled with thick sediments that thicken toward the frontal slope [e.g., *Ghosal et al.*, 2014; *Moeremans et al.*, 2014; *Geersen et al.*, 2015] (Figure S1). The seafloor is almost flat, and the sediment layers are laterally coherent, and likely indurated [*Dean et al.*, 2010; *Gulick et al.*, 2011; *Geersen et al.*, 2013]. Some buried channels as lenticular-shaped bodies of incoherent reflections have been found offshore northern Sumatra [*Mosher et al.*, 2008]. *Geersen et al.* [2015] identified three sedimentary units: Unit 1—the rapidly deposited trench wedge section composed of Bengal-Nicobar fan and forearc-derived sediments (0–4 Ma), Unit 2—a more gradually deposited section consisting of Nicobar fan sediments (4–40 Ma), and Unit 3—the slowly accumulated pelagic sediments at the bottom prior to the collision of India with Eurasia at ~40 Ma ago [*Curray et al.*, 1982]. The accurate ages of these sediments are pending drilling results. Due to the large thickness of the sediments, the basal sediments are likely to be subjected to high pressure and may be partially lithified; hence, they might be strengthened prior to accretion [*Dean et al.*, 2010; *Gulick et al.*, 2011; *Geersen et al.*, 2013]. On the other hand, besides the plate bending, this area is located in the actively deforming Wharton Basin, where the incoming plate is also affected by the reactivated fracture zones [e.g., *Deplus et al.*, 1998; *Carton et al.*, 2014; *Qin and Singh*, 2015; *Singh et al.*, 2017] that hosted several great earthquakes in 2012 (Figure 1) [e.g., *Wei et al.*, 2013]. Near the top of the basement, a high-amplitude negative polarity reflection packet (HANP) is observed [*Dean et al.*, 2010; *Ghosal et al.*, 2014] and interpreted as a predécollement that slips landward as a seismogenic décollement (a detachment fault at the base of the accretionary prism) [e.g., *Dean et al.*, 2010]. At the same time, this HANP layer could also relate to the frontal landward vergent thrust faults [*Moeremans et al.*, 2014]. Based

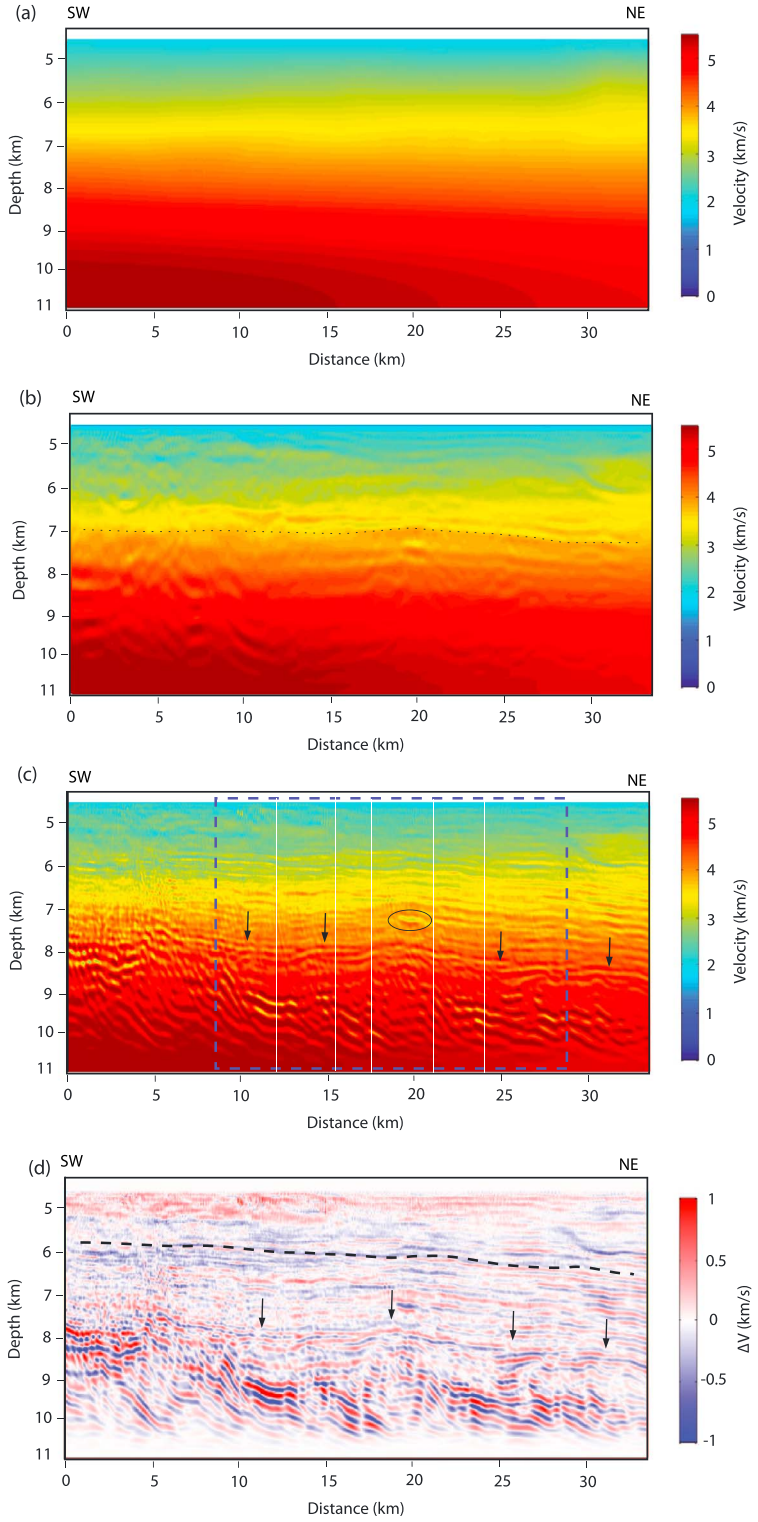

Figure 2. *P* wave velocity updated models during the FWI; the depths here are below sea level. (a) Starting model is constructed from high-resolution travel time tomographic results. (b) FWI result after step one; the dotted line indicates the possible diagenetic alteration place. (c) FWI result after step two; the blue dashed box marks the inverted area during step three, the black ellipse marks a low-velocity anomaly structure, the arrows mark the position of the HANP, and the white lines indicate the locations for the 1-D profiles in Figure 3. (d) Velocity anomaly section created by subtracting the starting model from the second step inverted result; the dashed line indicates a potential boundary for Units 1 and 2 sediments, and the arrows mark the position of the HANP.

on tomographic velocity model, *Ghosal et al.* [2014] classified three sedimentary layers in the oceanic plate section of this area down to ~8 km depth below the sea surface: an upper layer corresponding to a high-velocity gradient associated with uncompacted sediments, a low-velocity gradient layer associated with semi-compact sediments, and a second high-velocity gradient layer of highly compacted or crystalline sediments.

3. Seismic Reflection Data

We used a part of seismic profile WG2 that was acquired by WesternGeco's marine seismic vessel Geco Searcher in July 2006 [*Singh et al.*, 2008] (Figures 1 and S1), using a 12 km long Q-Marine [*Larsen et al.*, 2002] streamer towed at 15 m water depth. The seismic source was towed at 15 m water depth, which was composed of six subarrays with eight airguns in each subarray, providing a total array volume of 166.7 cubic liter. The shot interval was 50 m. The individual hydrophone spacing in the Q-Marine streamer was 3.125 m, and after digital noise attenuation and spatial anti-alias filtering [*Martin et al.*, 2000], the digital signals were spatially resampled to 12.5 m. The record length was 20.48 s with a temporal sample interval of 2 ms. Vessel speed varied from 2.2 to 2.5 m/s.

4. Inversion Methodologies

Full waveform inversion (FWI) is a powerful method to determine detailed velocity structures from seismic data. Our FWI scheme is based on the method proposed by *Shipp and Singh* [2002] to invert *P* wave velocity. The thick water layer (4.5 km) in our study area causes the refraction to arrive only at very far offsets in the original streamer data (at 11–12 km offset), limiting information about near surface velocity. A downward continuation (DC) technique [*Berryhill*, 1979, 1984] was used to extrapolate the surface seismic data to a subsurface at 200 m above the seafloor, allowing the refractions from shallow structures arriving as first arrivals that can be observed in the offset range of 0–9 km on the DC data [*Ghosal et al.*, 2014]. It also reduced ~6 s of the record length by removing the water layer, allowing to reduce the computational cost. Based on these data, we designed a three-step inversion strategy: (1) Step 1: FWI of far offset DC data (4–18 Hz; Figure S2) starting from the result of travel time inversion (Figure 2a), (2) Step 2: FWI of near offset DC reflection data (4–18 Hz; Figure S2), and (3) Step 3: FWI of near offset original surface streamer data (5–30 Hz) to obtain finer-scale information of the subsurface (see the supporting information for details).

The starting model for the inversion was obtained by combing the ray tracing tomographic results of the DC data [*Ghosal et al.*, 2014] and wide-angle ocean bottom seismometer data [*Singh et al.*, 2012] (Figure 2a). Before modeling, a 3-D to 2-D correction was applied [*Pica et al.*, 1990] by multiplying the real data by $\sqrt{t}$ and convolving with $1/\sqrt{t}$ to account for the geometrical spreading and phase adjustment, respectively. The source wavelet is obtained by stacking the nearest three traces of the seafloor reflector from several shots [*Collier and Singh*, 1997] and scaled by the amplitude ratio of the near offset reflectors between the synthetic and real data at the seafloor [*Brenders and Pratt*, 2007]. More details about the FWI can be found in the supporting information [*Fichtner et al.*, 2008; *Ghosal et al.*, 2014; *Lailly*, 1983; *Neves and Singh*, 1996; *Singh et al.*, 2012; *Tarantola*, 1984; *Virieux*, 1986].

5. Full Waveform Inversion Results

The velocity model obtained by step 1 contains medium-wavelength velocity structures, whereas those after Steps 2 and 3 provide short-wavelength structures (Figures 2 and 3). The far offset windowed data used in Step 1 contain the interference of wide-angle reflections and refraction arrivals; hence, the FWI provides a layered sedimentary model with alternating high and low velocities (Figure 2b) instead of a smooth model expected from the inversion of only turning ray arrivals. Furthermore, as the data contain reflections from the sediment-basement interface, the inversion has led to the development of the basement structure. This step fits most of middle-offset (3–7 km) wavefield (Figure S3). The result from Step 2 contains more detailed structures on short-wavelength scale (Figure 2c). Most near-offset reflected waves are fitted, particularly in the upper part (Figure S4). Sedimentary layers and the top of basement are clear, as well as the HANP (Figure 2c). Step 3 only focuses on a 20 km long segment (between 8 km and 28 km). Though the residuals were reduced by ~80% after the inversion (Figure S5), the final velocity model does not show a very big difference as compared to the previous model, suggesting that the step 2 results are robust. However, some

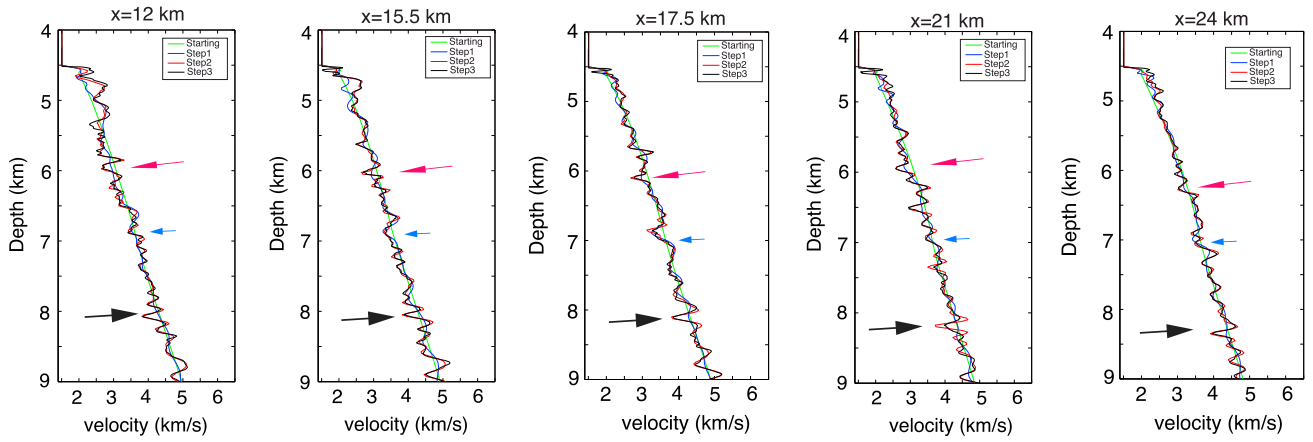

Figure 3. 1-D velocity profiles of starting model and inverted results in three steps along the model at different positions marked in Figure 2. The depths here are below sea level. The black arrows represent the HANP. The red arrows indicate the potential boundary of Units 1 and 2 sedimentary layers. The blue arrows indicate the possible diagenetic alteration between the low- and high-velocity layers.

shorter-wavelength scale structures have been included and the deep part is better constrained, which is evident from the 1-D velocity profiles (Figure 3).

The inversion results show that velocity increases to ~5 km/s at 9 km depth below the sea level (Figures 2 and 3). A low velocity associated with the HANP is present between 7.5 and 8.5 km depths (Figures 2c and 3). The HANP is ~70–80 m thick with a maximum velocity decrease of ~500 m/s (~4.0 km/s; Figure 3). This low-velocity layer is consistent with its negative polarity. The thickness estimation for the HANP is based on the inversion of seismic reflection data up to 30 Hz, but this layer could be thinner and a drilling would be required to quantify the precise thickness. We also find some low-velocity anomalies especially near $x = 20$ km at 7.5 km of depth, circled in Figure 2c, which may be due to the presence of fluid or gas since the velocity values reduce by ~1 km/s. At ~6 km depth, a layer with slightly low-velocity oscillation (~3 km/s; Figure 3) could be the boundary between different sedimentary units (Units 1 and 2) [*Geersen et al.*, 2015] formed at different periods. However, the boundary between Units 2 and 3 [*Geersen et al.*, 2015] is not very easy to be identified in the velocity profile; therefore, we assume that the HANP is the boundary. The high-velocity gradient at 8.5–9 km depth indicates the boundary between sediments and basalt (Figure 2). The basement complex topography in the southwest could be due to the presence of fracture zone F6 [*Carton et al.*, 2014].

We used the whole velocity model after Step 2 to perform Kirchhoff prestack depth migration of surface seismic reflection data. The velocity model and the seismic reflection image fit well in both depth (Figure 4) and time domains (Figure S6), including the sedimentary layers, the HANP, and the top of the oceanic crust, which indicates that the results are well constrained by the data. We can identify some high-angle conjugate normal faults that may be related to the diffuse deformation in Wharton Basin or plate bending.

6. Discussion and Conclusions

Our results provide insight about the sediment properties near the trench, with much higher resolution and accuracy than the previous velocity results in this [*Singh et al.*, 2012; *Ghosal et al.*, 2014] or nearby areas [*Dean et al.*, 2010; *Dessa et al.*, 2009; *Klingelhoefer et al.*, 2010]. In particular, we find a large decrease in velocity associated with the HANP, which could be due to high porosity and overpressured fluids [e.g., *Davis et al.*, 1983] that might lead to the formation of a protodécollement.

The upper part of the trench deposits (Units 1 and 2) are composed of northeastward gently dipping thick turbiditic sediments, with thickness increasing from ~3 km in the southwest to ~4 km in the northeast (Figure 4), corresponding to an average sedimentation rate of ~50–60 m/Ma. The shallow sediments could be affected by the fast deposition near the Bengal fan from late Pleistocene (~0.8 Ma) until Present [*Krishna et al.*, 2016]. Most of the high-angle normal faults lie below Unit 1, end at the boundary of Unit 1/2 (Figure 4), suggesting that the faults are nearly contemporaneous. These faults are probably related to the

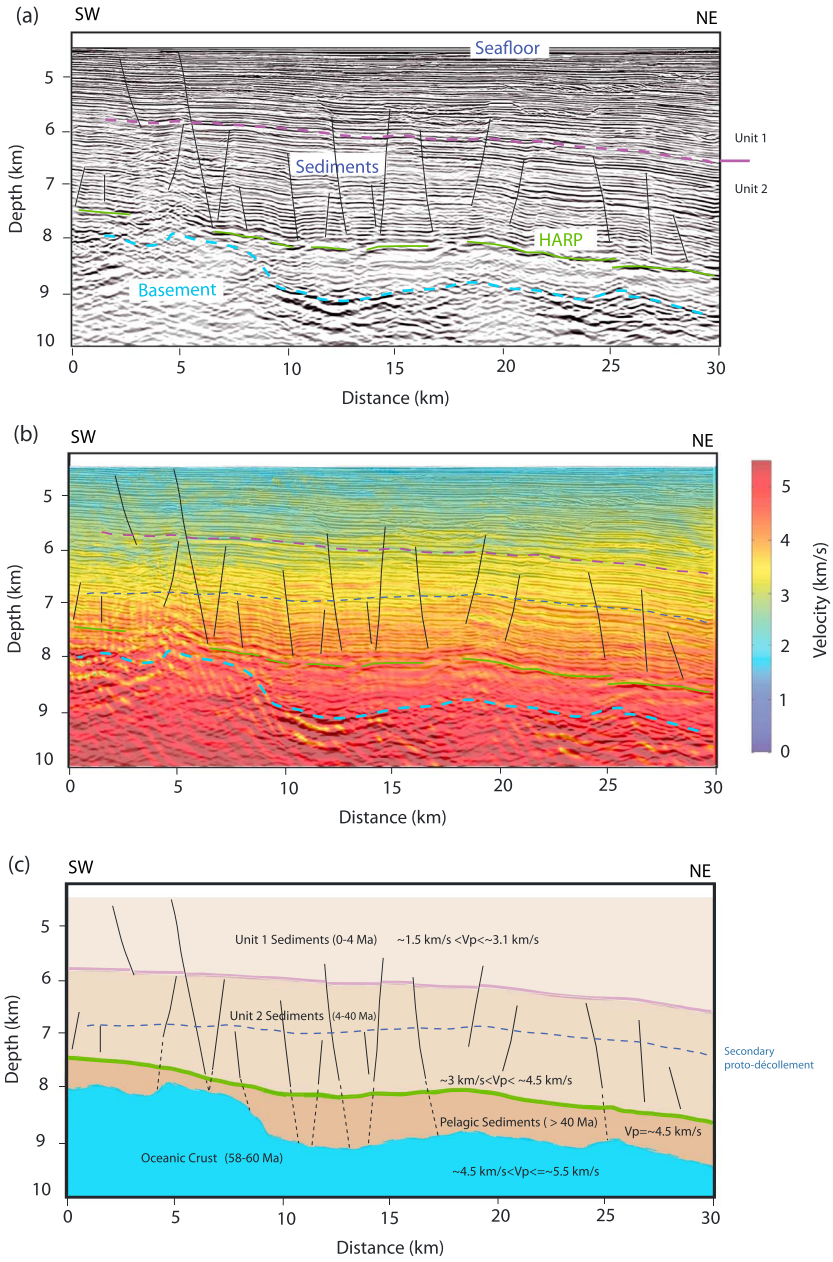

Figure 4. (a) Kirchhoff prestack depth-migrated image and its interpretation. The depths here are below sea level. The purple dashed line indicates the boundary between Units 1 and 2, the green lines represent the HANP, the blue dashed line marks the top of the oceanic crust, and near vertical black lines indicate faults. (b) Overlap of the migrated profile on the FWI inverted velocity model that is obtained after first two-step inversions. The dark blue dashed line indicates the possible diagenetic alteration layer that may be related to a second protodécollement. (c) A schematic diagram of our final model.

diffuse deformation in the Wharton Basin [e.g., *Geersen et al.*, 2015; *Graindorge et al.*, 2008; *Singh et al.*, 2017], or due to plate bending, which has also been found ~300 km south of our profile [*Franke et al.*, 2008] and in other subdution zones [e.g., *Ranero et al.*, 2003, 2005]. The active fault reaching the seafloor above the bathymetric high structures at the distance ~5 km might be related to the reactivation of fracture zone F6 [*Singh et al.*, 2011; *Qin and Singh*, 2015] or shear zones [*Singh et al.*, 2017]. In the sedimentary layers, there are some bright reflectors in the depth range of 6–7 km that correspond to low-velocity anomalies in the inverted velocity model (Figure 2), which might be related to channels that are caused by the lithology

and clay-type variations [*Han et al.*, 1986], or fluid accumulation due to the lithification and subsequent dehydration from the deeper layers [e.g., *Vrolijk et al.*, 1991]. Since this thick sedimentary layer has been accumulated over a long time period, it should be in thermal equilibrium with high temperature at its base over the 58 Ma old oceanic crust [*Jacob et al.*, 2014]. According to the earth cooling model [*McKenzie et al.*, 2005] and numerical computation [*Geersen et al.*, 2013], the temperature below ~7 km should be >60°C. This is the minimum temperature for smectite to illite transformation according to the data from laboratory experiments [*Kastner et al.*, 1991]. During this dewatering process, the normal faults in the sediments can act as pathways and enhance the transformation process [e.g., *Geersen et al.*, 2013].

The top Unit 1 thickens landward reaching to a thickness of ~2 km at the deformation front (Figure 4) with *P* wave velocity of 3.1 km/s at its base. This unit could include potential hemipelagic sediments (fan and forearc-derived sediments in the subduction environments) and gravity-flow deposits that contain turbidites [*McNeill et al.*, 2016a]. Unit 2 contains parallel high-amplitude reflections with a thickness of ~2 km at the deformation front, with the *P* wave velocity increasing from 3 km/s to ~4.5 km/s. In Unit 2, there are potentially well-drained silt- or sand-rich fan successions [*Gulick et al.*, 2011]. There seems to be a diagenetic alteration boundary at ~7 km depth where the velocity increases abruptly to ~3.8 km/s with a low-velocity layer above it (Figures 2b and 3). Above this depth, the velocity contours show a slightly upward tilt toward the deformation front in the northeast side, which is consistent with the first arrival travel time tomography result [*Ghosal et al.*, 2014], suggesting the effect of increased compaction toward the subduction front. Below the HANP, a weakly reflective sedimentary layer above the top of the basement (thickness up to ~0.8 km) has a *P* wave velocity of ~4.5–5 km/s, suggesting that this potentially clay- and silica-rich pelagic succession [*McNeill et al.*, 2016b] is highly compacted and lithified. This velocity is close to the velocity of pure clean quartz (> = 5000 m/s) [*Rider*, 2004], indicating that quartz could be a dominant material near the basement, which is also one of the subsidiary products during the illitization of smectite [e.g., *Niu et al.*, 2000]. Since we used turning waves in the inversion, which are sensitive to horizontal velocities, our inverted velocities could be ~10%–15% higher than the real vertical velocities. This could be due to the presence of anisotropy where the *P* wave velocity in the lateral direction is generally higher than that in the vertical direction.

Our results show that the HANP in the north Sumatra trench is a discrete layer, rather than a single interface between two units with contrasting seismic velocities. *Dean et al.* [2010] suggested that HANP could be the seaward extension of the décollement. Based on our 1-D velocity profiles (Figure 3), the HANP has the highest-velocity contrast within the sedimentary column. The thrust fault at the toe of the accretionary prism seems to intersect with the HANP (Figure S1), similar to the Simeulue area [*Dean et al.*, 2010]. However, the expected connected décollement cannot be seen beneath the accretionary wedge (Figure S1) [*Ghosal et al.*, 2014], which could be related to shearing at the toe of the prism [*Brown et al.*, 1994; *Moore et al.*, 1998]. The shearing of the décollement could disintegrate the décollement and contribute to the induration. The downward terminations of the thrust faults at the toe of the prism seem to be near the top of the basement (Figure S1), which is similar to the results found at ~200–300 km south off our study area [*Dean et al.*, 2010].

The HANP could be related to a lithological boundary [*Dean et al.*, 2010], the interface between turbiditic sediments above and pelagic sediments below [*Singh et al.*, 2008, 2011], or thin beds of sand and silt alteration [*Curray et al.*, 2003]. The pressure at the depth of HANP (3–4 km below seafloor) is more than 1.3 MPa [*Hüpers and Kopf*, 2012], and the temperature should be high enough (>60°C) for creating dewatering process in the deeper sediments [e.g., *Vrolijk et al.*, 1991] or upper crust [*Geersen et al.*, 2013]. *Geersen et al.* [2013] found that the base of the input section prior to subduction at northern Sumatra (<100 km north from our study area) may reach temperatures ≥90°C, which is sufficient to drive basement-related dehydration and other diagenetic reactions (e.g., clay mineral dehydration such as smectite-illite, grain assemblage alteration leading to cementation). Furthermore, the reactivated fracture zones F6 and F7 [*Carton et al.*, 2014; *Singh et al.*, 2017] and serpentinized upper mantle [*Qin and Singh*, 2015] are present in this area; they may lead to hydrothermal circulation in the crust and upper mantle providing heat for the smectite-illite transformation at the base of sediments. This dehydration transformation can supply SiO_2 at higher temperatures (70°C–200°C) [*Kameda et al.*, 2014], requiring some silica-rich succession near the basement [*McNeill et al.*, 2016b]. Our results show a large velocity drop caused by the HANP. If we assume a background velocity of 4.5 km/s associated with 4% of porosity [*Ghosal et al.*, 2014], then the porosity within the HANP would be ~30% containing overpressured fluid [*Taylor and Singh*, 2002]. These results are consistent with the drilling

data from the protodécollements and décollements in Barbados [*Moore et al.*, 1998; *Moore*, 2000] and Nankai Trough [e.g., *Ienaga et al.*, 2006]. This layer has also been interpreted as weak and fluid-rich materials in the dilatant fault zones [*Davis et al.*, 1983; *Shipley et al.*, 1994; *Bangs et al.*, 1999, 2010]. In our results, this fluid-rich thin layer that is located just above the strong coherent sediments on the basement may be a preferred slip surface during a megathrust earthquake and may act as a protodécollement.

The top of the HANP has a high velocity, indicating the presence of a strong roof capable of trapping fluid in this high-porosity layer under high fluid pressure. The overpressured fluid can restrain the velocity weakening, and thermally pressurized fluids that come from the crust could also contribute to the dynamical weakening in the trench area [*Hirono et al.*, 2016]. The sediments between the HANP and basement have a high velocity (~4.5 km/s; Figures 3 and 4), suggesting that the sediments are highly compacted and lithified, and behave as a part of the subducting oceanic crust. During the subduction process, the sediments above the HANP would be accreted, whereas the indurated part below the HANP would be subducted along with the basement. The weak HANP could play the role of a subduction channel, acting as a décollement beneath the forearc. Due to the increasing shear stress and temperature along the megathrust at a certain depth, the fluid in the subducting channel would be released and migrate toward the subduction front accumulating within the HANP. On the other hand, the potentially quartz at the base of sediments that have been discussed before can lead to a velocity weakening [e.g., *Ikari et al.*, 2011] and its cementation will cause progressive lithification of the décollement zone [*Byrne*, 1998; *Moore and Saffer*, 2001]. Hence, the deeply buried décollement could result in the updip extension of velocity weakening rheology up to the front and extend the coseismic rupture to the front during an earthquake such as the 2004 event as suggested by other studies [e.g., *Gulick et al.*, 2011]. The thick and strong incoming sediments could efficiently transfer seismic energy into motion of the overlying seafloor over a large area in the deep water during the coseismic rupture reaching the Sunda Trench, leading to an enhanced tsunami.

Furthermore, we observed two sets of the normal faults in the seismic image (Figure 4). The upward terminations of the first set are close to the Unit 1 base and the second set terminates near the low-velocity layer above the diagenetic alteration boundary at ~7 km depth. These faults can provide pathways for fluids moving up from the deep areas, creating low-velocity layers. The boundary between Units 1 and 2 is ~2 km above the basement, where the velocity variation is small as compared to that in the HANP, hence, currently it is not weak enough to host a major protodécollement. However, the reflections corresponding to the diagenetic alteration boundary are close to the place where the pop-up structure at the toe of prism initiates (Figures S1and 4b). Thus, the low-velocity layer could develop a secondary décollement in the accretionary wedge, which has been observed off the central Sumatra [*Kuncoro et al.*, 2015], acting as a conveyer belt in preserving the pop-up structures. The diagenetic harder materials just below this low-velocity layer could act as a base sedimentary layer of the pop-up structures beneath the forearc, involved in dehydration process and gradually indurated. Figure 4c shows a schematic diagram describing our results.

We conclude from the FWI results that the bottom of the thick trench-fill sediments has been highly compacted, overlain by a thin fluid-rich layer HANP, which is the product of joint action of geothermal activities and shear stress loading along the subduction interface, acting as the protodécollement. The accretionary wedge with indurated décollement at the plate interface requires a strong coupling, leading to the frontal rupture during a megathrust earthquake and enhancing the tsunami. The weak layer in the middle of sedimentary layer could develop a second décollement and contribute to the pop-up structures building in the accretionary wedge.

Acknowledgments
We thank WesternGeco for providing the data. Numerical computations were performed on the S-CAPAD platform, IPGP, France. Seismic data and FWI results can be obtained on request. All data needed to evaluate the conclusions in the paper are present in the paper and/or the supporting information.

References

Ammon, C. J., et al. (2005), Rupture process of the 2004 Sumatra-Andaman earthquake, *Science*, *308*(5725), 1133–1139.
Bangs, N. L., T. H. Shipley, J. C. Moore, and G. F. Moore (1999), Fluid accumulation and channeling along the northern Barbados Ridge Décollement Thrust, *J. Geophys. Res.*, *104*, 20,399–20,414, doi:10.1029/1999JB900133.
Bangs, N. L., M. J. Hornbach, G. F. Moore, and J.-O. Park (2010), Massive methane release triggered by seafloor erosion offshore southwestern Japan, *Geology*, *38*, 1019–1022, doi:10.1130/G31491.1.
Berryhill, J. R. (1979), Wave equation datuming, *Geophysics*, *44*, 1329–1344.
Berryhill, J. R. (1984), Wave-equation datuming before stack, *Geophysics*, *49*, 2064–2066.
Brenders, A., and R. Pratt (2007), Full waveform tomography for lithospheric imaging: Results from a blind test in a realistic crustal model, *Geophys. J. Int.*, *168*, 133–151.
Brown, K. M., B. Bekins, B. Clennell, D. Dewhurst, and G. Westbrook (1994), Heterogeneous hydrofracture development and accretionary fault dynamics, *Geology*, *22*, 259–262.

Byrne, T. (1998), Seismicity, slate belts and coupling along convergent plate boundaries, *Eos Trans. AGU*, *79*, W-114.
Carton, H., S. C. Singh, N. D. Hananto, J. Martin, Y. S. Djajadihardja, D. F. Udrekh, and C. Gaedicke (2014), Deep seismic reflection images of the Wharton Basin oceanic crust and uppermost mantle offshore northern Sumatra: Relation with active and past deformation, *J. Geophys. Res. Solid Earth*, *119*, 32–51, doi:10.1002/2013JB010291.
Chester, F. M., Mori, J. J., Toczko, S., Eguchi, N., and the Expedition 343/343T Scientists (2012), Japan Trench Fast Drilling Project (JFAST), *IODP Prel. Rept*., 343/343T, doi:10.2204/iodp.pr.343343T.
Collier, J. S., and S. C. Singh (1997), Detailed structure of the top of the melt body beneath the East Pacific Rise at 9°40′N from waveform inversion of seismic reflection data, *J. Geophys. Res.*, *1022*, 20,287–20,304, doi:10.1029/97JB01514.
Curray, J. R., F. J. Emmel, D. G. Moore, and R. W. Raitt (1982), Structure, tectonics and geological history of the northeastern Indian Ocean, in *The Ocean Basins and Margins*, *The Indian Ocean*, vol. 6, edited by A. E. Nairn and F. G. Stheli, pp. 399–450, Plenum, New York.
Curray, J. R., F. J. Emmel, and D. G. Moore (2003), The Bengal fan: Morphology, geometry, stratigraphy, history and processes, *Mar. Petro. Geol.*, *19*, 1191–1223.
Davis, D., J. Suppe, and F. A. Dahlen (1983), Mechanics of fold and thrust belts and accretionary wedges, *J. Geophys. Res.*, *88*, 1153–1172, doi:10.1029/JB088iB02p01153.
Dean, S. M., L. C. McNeill, T. J. Henstock, J. M. Bull, S. P. S. Gulick, J. A. Austin Jr., N. L. B. Bangs, Y. S. Djajadihardja, and H. Permana (2010), Contrasting décollement and prism properties over the Sumatra 2004–2005 earthquake rupture boundary, *Science*, *329*, 207–210.
Deplus, C., M. Diament, H. Hébert, G. Bertrand, S. Dominguez, J. Dubois, J. Malod, P. Patriat, B. Pontoise, and J.-J. Sibilla (1998), Direct evidence of active deformation in the eastern Indian oceanic plate, *Geology*, *26*, 131–134.
Dessa, J.-X., F. Klingelhoefer, D. Graindorge, C. André, H. Permana, M.-A. Gutscher, A. Chauhan, S. C. Singh, and the SUMATRA-OBS Scientific Team (2009), Megathrust earthquakes can nucleate in the forearc mantle: Evidence from the 2004 Sumatra event, *Geology*, *37*, 659–662.
Fichtner, A., B. L. N. Kennett, H. Igel, and H. P. Bunge (2008), Theoretical background for continental- and global-scale full-waveform inversion in the time-frequency domain, *Geophys. J. Int.*, *175*, 665–685.
Franke, D., M. Schnabel, S. Ladage, D. Tappin, S. Neben, Y. S. Djajadihardja, C. Muller, H. Kopp, and C. Gaedicke (2008), The great Sumatra-Andaman earthquakes—Imaging the bondary between the ruptures of the great 2004 and 2005 earthquakes, *Earth Planet. Sci. Lett.*, *269*, 119–130.
Geersen, J., L. McNeill, T. J. Henstock, and C. Gaedicke (2013), The 2004 Aceh-Andaman earthquake: Early clay dehydration controls shallow seismic rupture, *Geochem., Geophys. Geosyst.*, *14*, 3315–3323, doi:10.1002/ggge.20193.
Geersen, J., J. M. Bull, L. C. McNeill, T. J. Henstock, C. Gaedicke, N. Chamot-Rooke, and M. Delescluse (2015), Pervasive deformation of an oceanic plate and relationship to large $> M_w$ 8 intraplate earthquakes: The northern Wharton Basin, Indian Ocean, *Geology*, doi:10.1130/G36446.1.
Ghosal, D., S. C. Singh, and J. Martin (2014), Shallow subsurface morphotectonics of the NW Sumatra subduction system using an integrated seismic imaging technique, *Geophys. J. Int.*, *198*, 1818–1831.
Graindorge, D., et al. (2008), Impact of lower plate structure on upper plate deformation at the NW Sumatran convergent margin from seafloor morphology, *Earth Planet. Sci. Lett.*, *275*, 201–210.
Gulick, S., J. Austin, L. McNeill, N. Bangs, K. Martin, T. Henstock, J. Bull, S. Dean, Y. Djajadishardja, and H. Permana (2011), Thick indurated sediments extend updip rupture propagation during 2004 Sumatra earthquake, *Nat. Geosci.*, *4*, 453–456.
Han, D., A. Nur, and D. Morgan (1986), Effect of porosity and clay content on wave velocity in sandstones, *Geophysics*, *51*, 2093–2107.
Henstock, T. J., L. C. McNeill, and D. R. Tappin (2006), Seafloor morphology of the Sumatran subduction zone: Surface rupture during megathrust earthquakes?, *Geology*, *34*, 485–488.
Hirono, T., K. Tsuda, W. Tanikawa, J. P. Ampuero, B. Shibazaki, M. Kinoshita, and J. J. Mori (2016), Near-trench slip potential of megaquakes evaluated from fault properties and conditions, *Sci. Rep.*, doi:10.1038/srep28184.
Hüpers, A., and A. J. Kopf (2012), Effect of smectite dehydration on pore water geochemistry in the shallow subduction zone: An experimental approach, *Geochem. Geophys., Geosyst.*, *13*, Q0AD26, doi:10.1029/2012GC004212.
Ienaga, M., L. C. McNeill, H. Mikada, S. Saito, D. Goldberg, and J. C. Moore (2006), Borehole image analysis of the Nankai Accretionary Wedge, ODP Leg 196: Structural and stress studies, *Tectonophysics*, *426*, 207–220.
Ikari, M. J., C. Marone, and D. M. Saffer (2011), On the relation between fault strength and frictional stability, *Geology*, *39*, 83–86.
Jacob, J., J. Dyment, and V. Yatheesh (2014), Revisiting the structure, age, and evolution of the Wharton Basin to better understand subduction under Indonesia, *J. Geophys. Res. Solid Earth*, *119*, 169–190, doi:10.1002/2013JB010285.
Kameda, J., K. Kawabata, Y. Hamada, A. Yamaguchi, and G. Kimura (2014), Quartz deposition and its influence on the deformation process of megathrusts in subduction zones, *Earth Planets Space*, *66*, 13.
Kastner, M., H. Elderfield, and J. B. Martin (1991), Fluids inconvergent margins: What do we know about their composition, origin, role in diagenesis and importance for oceanic chemical fluxes?, *Philos. Trans. R. Soc.*, *335*(1638), 243–259.
Klingelhoefer, F., M.-A. Gutscher, S. Ladage, J.-X. Dessa, D. Graindorge, D. Franke, C. André, H. Permana, T. Yudistira, and A. Chauhan (2010), Limits of the seismogenic zone in the epicentral region of the 26 December 2004 great Sumatra-Andaman earthquake: Results from seismic refraction and wide-angle reflection surveys and thermal modeling, *J. Geophys. Res.*, *115*, B01304, doi:10.1029/2009JB006569.
Konca, A. O., et al. (2008), Partial rupture of locked patch of the Sumatra megathrust during the 2007 earthquake sequence, *Nature*, *456*, 631–635.
Krishna, K. S., M. Ismaiel, K. Srinivas, D. Gopala Rao, J. Mishra, and D. Saha (2016), Sediment pathways and emergence of Himalayan source material in the Bay of Bengal, *Curr. Sci.*, *110*, 363–372.
Kuncoro, A. K., N. Cubas, S. C. Singh, M. Etchebes, and P. Tapponnier (2015), Tsunamigenic potential due to frontal rupturing in the Sumatra locked zone, *Earth Planet. Sci. Lett.*, *432*, 311–322.
Lailly, P. (1983), The seismic inverse problem as a sequence of before stack migrations: Conference on Inverse Scattering, Theory and Application, *Society for Industrial and Applied Mathematics*, *Expanded Abstracts*, 206–220.
Larsen, L., et al. (2002), Q-Marine seismic acquisition results: Report from WesternGeco, *First Break*, *20*.
Liu, C. S., J. R. Curray, and J. M. McDonald (1983), New constraints on the tectonic evolution of the eastern Indian Ocean, *Earth Planet. Sci. Lett.*, *65*, 331–342.
Martin, J., A. Özbek, L. Combee, N. Lunde, S. Bittleson, and E. Kragh (2000), Acquisition of marine point receiver data with a towed streamer, *Society of Exploration Geophysicists*, *Expanded Abstracts ACQ3.3*.
McKenzie, D., J. Jackson, and K. Priestley (2005), Thermal structure of oceanic and continental lithosphere, *Earth Planet. Sci. Lett.*, *233*, 337–349.
McNeill, L., B. Dugan, and K. Petronotis (2016a), *Expedition 362 Scientific Prospectus: The Sumatra Subduction Zone*, International Ocean Discovery Program, Tex., doi:10.14379/iodp.sp.362.2016.

McNeill, L., et al. (2016b), *The Sumatra Subduction Zone—The Role of Input Materials in Shallow Seismogenic Slip and Forearc Plateau Development*, International Ocean Discovery Program, IODP Proposal 837 full.
Moeremans, R., S. C. Singh, M. Mukti, J. McArdle, and K. Johansen (2014), Seismic images of structural variations along the deformation front of the Andaman-Sumatra subduction zone: Implications for rupture propagation and tsunamigenesis, *Earth Planet. Sci. Lett.*, *386*, 75–85.
Moore, J. C. (2000), Synthesis of results: logging while drilling, northern Barbados accretionary prism, in *Proc. Ocean Drilling Program, Science Results*, 171A, edited by J. C. Moore and A. Klaus, pp. 1–25, College Station, Tex., doi:10.2973/odp.proc.sr.171a.101.2000.
Moore, J. C., and D. M. Saffer (2001), Updip limit of the seismogenic zone beneath the accretionary prism of southwest Japan: An effect of diagenetic to low-grade metamorphic processes and increasing effective stress, *Geology*, *29*, 183–186.
Moore, J. C., et al. (1998), Consolidation patterns during initiation and evolution of a plate-boundary décollement zone: Northern Barbados accretionary prism, *Geology*, *26*(9), 811–814.
Mosher, D. C., J. A. Austin Jr., D. Fisher, and S. P. S. Gulick (2008), Deformation of the northern Sumatra accretionary prism from high-resolution seismic reflection profiles and ROV observations, *Mar. Geol.*, *252*, 89–99.
Neves, F. A., and S. C. Singh (1996), Sensitivity study of seismic reflection/refraction data, *Geophys. J. Int.*, *126*, 470–476.
Niu, B., T. Yoshimura, and A. Hirai (2000), Smectite diagenesis in Neogene marine sandstone and mudstone of the Niigata Basin, Japan, *Clays Clay Miner.*, *48*, 26–42.
Pica, A., J. P. Diet, and A. Tarantola (1990), Nonlinear inversion of seismic reflection data in a laterally invariant medium, *Geophysics*, *55*, 284–292.
Qin, Y., and S. C. Singh (2015), Seismic evidence of a two-layer lithospheric deformation in the Indian Ocean, *Nat. Commun.*, *6*, doi:10.1038/ncomms9298.
Ranero, C. R., J. Phipps Morgan, K. McIntosh, and C. Reichert (2003), Bending-related faulting and mantle serpentinization at the Middle America trench, *Nature*, *425*, 367–373.
Ranero, C. R., A. Villasenor, J. Phipps Morgan, and W. Weinrebe (2005), Relationship between bend faulting at trenches and intermediate-depth seismicity, *Geochem. Geophys. Geosyst.*, *6*, Q12002, doi:10.1029/2005GC000997.
Rider, M. (2004), *The Geological Interpretation of Well Logs*, French Rider Consult, Scotland.
Shipley, T. H., G. F. Moore, N. L. Bangs, J. C. Moore, and P. L. Stoffa (1994), Seismically inferred dilatancy distribution, northern Barbados Ridge décollement: Implications for fluid migration and fault strength, *Geology*, *22*, 411–414.
Shipp, R., and S. C. Singh (2002), Two-dimensional full wavefield inversion of wide-aperture marine seismic streamer data, *Geophys. J. Int.*, *151*, 324–344.
Singh, S., et al. (2008), Seismic evidence for broken oceanic crust in the 2004 Sumatra earthquake epicentral region, *Nat. Geosci.*, *1*, 777–781.
Singh, S. C., H. Carton, A. P. S. Chauhan, S. Androvandi, A. Davaille, J. Dyment, M. Cannat, and N. Hananto (2011), Extremely thin crust in the Indian ocean possibly resulting from the Plume-Ridge interaction, *Geophys. J. Int.*, *184*, 29–42.
Singh, S. C., A. P. S. Chauhan, A. J. Calvert, N. D. Hananto, D. Ghosal, A. Rai, and H. Carton (2012), Seismic evidence of bending and unbending of subducting oceanic crust and the presence of mantle megathrust in the 2004 Great Sumatra earthquake rupture zone, *Earth Planet. Sci. Lett.*, *321–322*, 166–176, doi:10.1016/j.epsl.2012.01.012.
Singh, S. C., et al. (2017), The discovery of a conjugate system of faults in the Wharton Basin intra-plate deformation zone, *Sci. Adv.*, *3*, e1601689, doi:10.1126/sciadv.1601689.
Tarantola, A. (1984), Inversion of seismic reflection data in the acoustic approximation, *Geophysics*, *49*, 1259–1266.
Tarantola, A. (1986), A strategy for nonlinear elastic inversion of seismic reflection data, *Geophysics*, *51*, 1893–1903.
Taylor, M. A. J., and S. C. Singh (2002), Composition and microstructure of magma bodies from effective medium theory, *Geophys. J. Int.*, *149*, 15–21.
Virieux, J. (1986), P-SV wave propagation in heterogeneous media: Velocity-stress finite difference method, *Geophysics*, *51*, 889–901.
Vrolijk, P., A. Fisher, and J. Gieskes (1991), Geochemical and geothermal evidence for fluid migration in the Barbados accretionary prism (ODP leg 110), *Geophys. Res. Lett.*, *18*, 947–950, doi:10.1029/91GL00913.
Wang, K., and Y. Hu (2006), Accretionary prisms in subduction earthquake cycles: The theory of dynamic Coulomb wedge, *J. Geophys. Res.*, *111*, B06410, doi:10.1029/2005JB004094.
Wei, S., D. Helmberger, and J.-P. Avouac (2013), Modeling the 2012 Wharton Basin earthquake off Sumatra; Complete lithospheric failure, *J. Geophys. Res. Solid Earth*, *118*, 3592–3609, doi:10.1002/jgrb.50267.